electronics

Article

# Flexible Frequency Response Strategy with Smooth Rotor Speed Recovery of a DFIG-Based Wind Turbine

**Xiaocen Xue [1], Shun Sang [1,2] and Jiejie Huang [1,*]**

[1] School of Electric Engineering, Nantong University, Nantong 226010, China
[2] State Key Laboratory of Operation and Control of Renewable Energy & Storage Systems, China Electric Power Research Institute, Beijing 100192, China
* Correspondence: huangjiejie@ntu.edu.cn

**Abstract:** Grid frequency must be regulated in its nominal range to guarantee the stable operation of an electric power grid. Excessive grid frequency excursions result in load shedding, grid frequency instability, or even synchronous generator damage. With the growing wind penetration, there is an increasing issue about the reduction in inertia response. This paper addresses a self-adaptive inertial control strategy for improving the frequency nadir and smoothly regaining the rotor speed to the initial working condition without causing a second frequency drop (SFD). The first objective is achieved by determining the incremental power considering the maximum rate of change of frequency; the secondary goal is realized by smoothly decreasing the power reference based on the decreasing function. Simulation results verify that the proposed control strategy not only boosts the frequency nadir but also guarantees the smooth rotor speed recovery with a negligible SFD.

**Keywords:** frequency support; inertial control; power system control; DFIG; kinetic energy; rotor speed recovery



**Citation:** Xue, X.; Sang, S.; Huang, J. Flexible Frequency Response Strategy with Smooth Rotor Speed Recovery of a DFIG-Based Wind Turbine. *Electronics* **2023**, *12*, 794. https://doi.org/10.3390/electronics12040794

Academic Editors: Marco Mussetta, Dinh Duong Le and Minh Quan Duong

Received: 17 January 2023
Revised: 30 January 2023
Accepted: 3 February 2023
Published: 5 February 2023



## 1. Introduction

The electric power system should keep the system frequency at an acceptable level [1]. It is required to provide frequency response capabilities against disturbances; otherwise, the grid frequency excursions might lead to load shedding, grid frequency instability, or even synchronous generator damage [2]. Variable-speed wind turbine generators (VSWTGs), e.g., doubly fed induction generators (DFIGs), achieve a maximum power point tracking (MPPT) operation at different wind speed conditions. Nevertheless, VSWTGs rarely contribute inertia and primary frequency responses since they are not synchronous to the power grid and have no reserve power [3]. The lower system inertia and displacement of primary frequency response result in the severe rate of change of frequency, low frequency nadir and steady-state frequency, and further increasing the possibility to cause activations of relays, e.g., under-frequency load shedding. This might translate to a decline in the power system stability and reliability [3–5]. Some countries have headlined the requirements on the inertial control of VSWTGs [6,7]. The capability for releasing kinetic energy from the DFIG is more than that from conventional synchronous fleets, and thus, the DFIG or DFIG-based wind farm can be a better option for frequency support [8].

Inertial control, which is a type of frequency support function of a DFIG, can be primarily divided into two classifications that enable the DFIG to support the system frequency: stepwise inertial control and frequency-based inertial control. Frequency-based inertial control is implemented on the basis of the rate of change of frequency, frequency excursion, or a combination of both [9–11]. Special attention should be paid to setting the control coefficients [12]. Stepwise inertial control (SIC) is implemented on the basis of the predetermined function [13–20]. SIC is able to boost the frequency nadir at a high level compared to that of frequency-based inertial control by injecting a fast and large amount of output power [14]. However, the incremental power only varies with operating conditions, but it is not suitable for various disturbances, so that the frequency nadir could not be improved effectively. Further, the second frequency drop (SFD) issues tend to occur when the DFTG quits the frequency support period [15].

The authors of [16] indicate that SFD can be prevented or reduced by avoiding the sudden decrease in active power of the DFIG. To reduce the sudden power decrease, many solutions are proposed in [17–20]. In [17], a novel power reference function is addressed that decrease output power with a preset slope. However, the parameters are heuristically determined so that they are valid only for a specific generation mix of a power system and power system condition. In [18], a linear function method is addressed that instantly decreases an amount of power, so the SFD is inevitable. The above schemes suggest a comprehensive nonlinear function, which is difficult to be implemented into the controller. The authors of [9] address a two-level variable coefficient to mitigate the SFD; however, the effectiveness mainly depends on the predetermined training of the fuzzy controller. The authors of [19] reduce a small constant after the rotor speed converges. Even though this scheme reduces the size of SFD, it delays the rotor speed recovery, and further results in annual production loss of wind power. To quicken the rotor speed while reducing the SFD, an adaptive power reference is proposed in [20], however, the frequency nadir is unable to be improved effectively.

Based on the shortcoming of the existing frequency response strategies, the main contributions of this research are as follows:

- Different stepwise inertial control schemes are analyzed.
- The incremental power of the proposed scheme is calculated based on the maximum $df_{sys}/dt$.
- The rotor speed recovery strategy is proposed to address the second frequency drop and speed recovery.

This paper addresses a self-adaptive inertial control scheme of the DFIG, which is designed to boost the frequency nadir at a high level and ensure the smooth rotor speed restoration with a negligible SFD. Furthermore, DFIGs are assumed to work at MPPT mode without reserve power, and the kinetic energies in the wind turbines are employed to support the system frequency. Dynamic performances of the proposed self-adaptive inertial control strategy are evaluated.

## 2. Modeling of a Doubly Fed Induction Generator

The main components of the DFIG consist of a wind turbine model, gear box, induction generator, and power electronic converters including rotor-side and grid-side converters.

As shown in Figure 1, the goal of the rotor-side converter is to regulate the active power, including maximum power point tracking operation and frequency control, but it also regulates the reactive power in the stator of the DFIG. The goal of the grid-side converter is to regulate the voltage of the DC link [21].

Equations (1)–(4) illustrate the dynamics of the wind turbine, where $P_m$, $R$, $\beta$, $\rho$, $c_p$, $v_w$, and $\lambda$ represent extracted mechanical power, rotor radius, pitch angle, air density, power coefficient, wind speed, and tip speed ratio, respectively. Further, a two-mass system is employed to indicate the rotational dynamics of the wind turbine, gear box, and induction generator [22].

$$P_m = 0.5\rho\pi R^2 v_w^3 c_P(\lambda,\beta) \tag{1}$$

$$c_P(\lambda,\beta) = 0.645\left\{0.00912\lambda + \frac{-5-0.4(2.5+\beta)+116\lambda_i}{e^{21\lambda_i}}\right\} \tag{2}$$

$$\lambda_i = \frac{1}{\lambda+0.08(2.5+\beta)} - \frac{0.035}{1+(2.5+\beta)^3} \tag{3}$$

$$\lambda = \frac{\omega_r R}{v_w}. \tag{4}$$

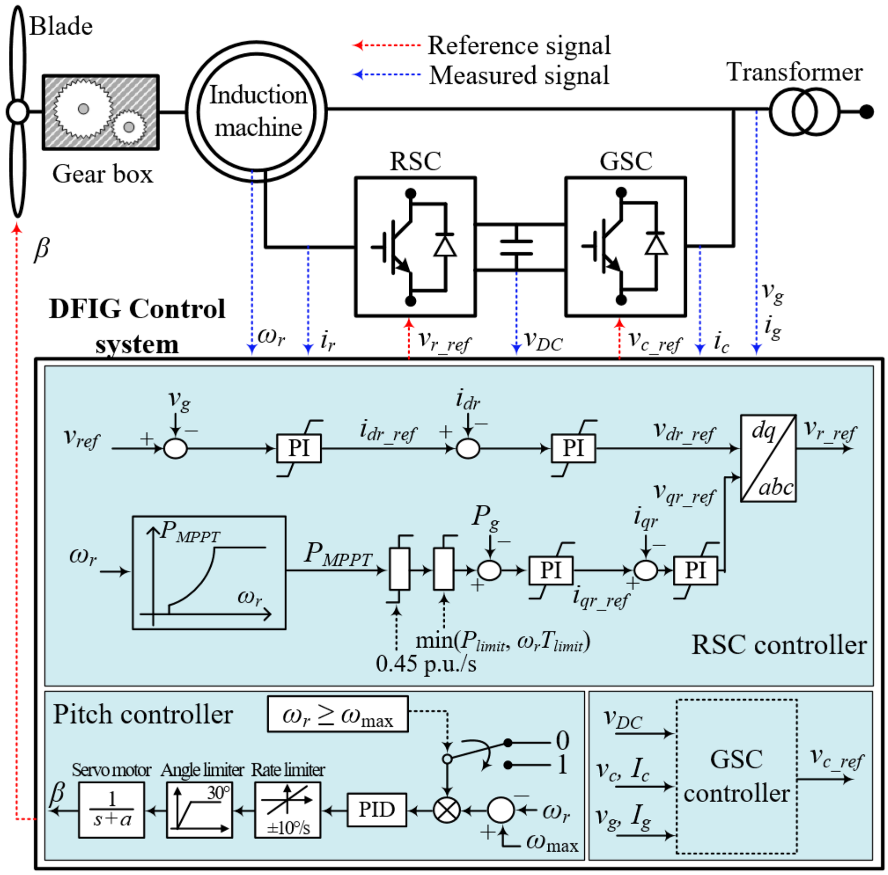


**Figure 1.** Simplified configuration of a DFIG model.

At the optimal tip speed ratio ($\lambda_{opt}$), $c_p$ retains a maximum value to achieve MPPT. The MPPT operation reference is represented by

$$P_{MPPT} = 0.5\rho\pi R^2 \left(\frac{\omega_r R}{\lambda_{opt}}\right)^3 c_{p,\max} = k_g \omega_r^3 \tag{5}$$

where $\omega_r$ is the rotor speed; $c_{p,\max}$ is the maximum value when $\beta$ = 0°; $\lambda_{opt}$ is the optimal value of $\lambda$ [23]; and $k_g$ is constant.

In addition, the MPPT operation could be achieved by the optimal tip speed ratio, power signal feedback method, mountain climbing method, and fuzzy control, as suggested in [24,25]. In this paper, the optimal tip speed ratio is employed.

## 3. Stepwise Inertial Control of a DFIG for System Frequency Support

Figure 2 depicts the control concept of SIC. When detecting a disturbance, the power reference switches to the power reference function, which includes the power references for frequency supporting stage and rotor speed recovery.

### 3.1. Conventional Inertial Control for System Frequency Support

This subsection briefly introduces the concepts of SIC methods for supporting the system frequency in [13,19,20], which are represented as SIC #1, SIC #2, and SIC #3, respectively.

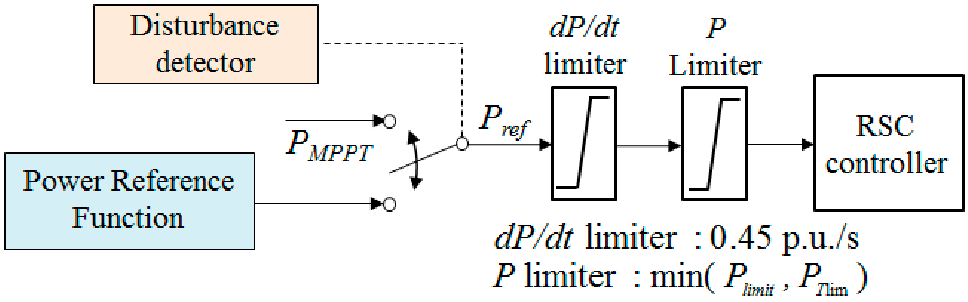


**Figure 2.** Control concept of SIC.

#### 3.1.1. SIC #1

After detecting a frequency disturbance ($t_0$), SIC #1 switches the power reference ($P_{ref}$) to $P_{SIC}$, which is the power reference during inertia control. $P_{SIC}$ for SIC #1 is calculated by $P_0 + \Delta P$, where $\Delta P$ is the additional power injection for inertia control and is maintained for the deceleration period, $t_{\text{dec}}$. At $t_0 + t_{\text{dec}}$, $P_{SIC}$ instantly declines from $P_0 + \Delta P$ to $P_0 - 0.5\Delta P$ and is kept for the acceleration period, $t_{acc}$ (see in Figure 3a,b); at $t_0 + t_{\text{dec}}$, a significant SFD might occur. For low wind speed conditions, over-deceleration might be caused, which results in a significant SFD; to avoid this, $\Delta P$ is suggested to be set to a small value. The $t_{\text{dec}}$ and $t_{acc}$ are set to 10.0 s and 20.0 s, respectively. At $t_0 + t_{\text{dec}} + t_{acc}$, $P_{ref}$ is returned to the MPPT curve. The trajectory of this method is A-B-C-D-E-A, as shown in Figure 3. $P_{ref}$ of SIC #1 in the time domain can be summarized as in (6).

$$P_{ref} = \begin{cases} P_0 + \Delta P_{FS} & t_0 \leq t \leq t_0 + t_{\text{dec}} \\ P_0 - 0.5\Delta P_{FS} & t_0 + t_{\text{dec}} \leq t \leq t_0 + t_{\text{dec}} + t_{acc} \\ P_{MPPT} & t_0 + t_{\text{dec}} + t_{acc} \leq t \end{cases} \tag{6}$$

Implementation of SIC #1 may face the following challenges: (I) the magnitude of $\Delta P$ is set to 0.1 p.u. and 0.05 p.u for high and low wind speed conditions, respectively, which restrict the dynamic frequency supporting performance of the SIC method against various disturbances under different wind conditions. (II) The power reduction from the frequency support stage to the $\omega_r$ recovery stage (trajectory from C to E in Figure 3) results in a severe SFD to the grid. (III) During the $\omega_r$ recovery stage, $P_{ref}$ in the time domain may impose instability issues if sudden disturbance occurs, i.e., wind speed decreases.

#### 3.1.2. SIC #2

Figure 4 depicts the power reference of SIC #2. To boost the frequency nadir, the power reference of the frequency support stage increases from $P_{MPPT}$ to $\Delta P + P_{MPPT}$. $P_{SIC}$ decreases with the decreasing $\omega_r$ until the operating point moves to Point C in Figure 4, in which $P_{SIC}$ equals $P_m$. This indicates that SIC #2 avoids over-deceleration even when a large $\Delta P$ is used and the frequency supporting stage ends.

During the $\omega_r$ recovery stage, to regain the rotor speed, SIC #2 instantly reduces the power reference by a constant value, $\Delta P_{\text{RR}}$ (which is 0.03 p.u., suggested in [17]), and then keeps $P_{MPPT}(\omega_C) - 0.03$ p.u until $P_{SIC}$ intersects the MPPT curve, as shown in Figure 4. At Point D, $P_{ref}$ is changed back to $P_{MPPT}$; thereafter, $\omega_r$ is restored to $\omega_0$. The trajectory of SIC #2 is A-B-C-D-E-A, as shown in Figure 4. The power reference of SIC #2 can be summarized as in (7).

$$P_{ref} = \begin{cases} P_{MPPT} + \Delta P_{FS} & \omega_C \leq \omega_r \leq \omega_0 \\ P_{MPPT}(\omega_C) - 0.03 & \omega_C \leq \omega_r \leq \omega_D \\ P_{MPPT} & \omega_D \leq \omega_r \end{cases} \tag{7}$$

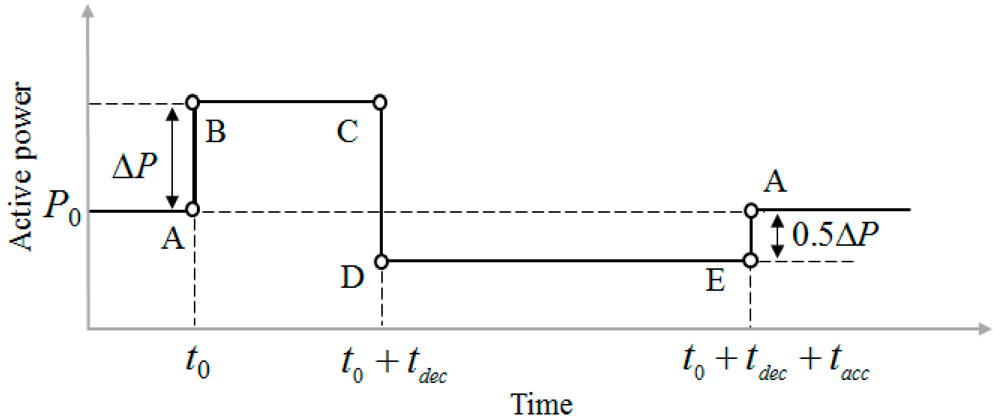


(**a**)

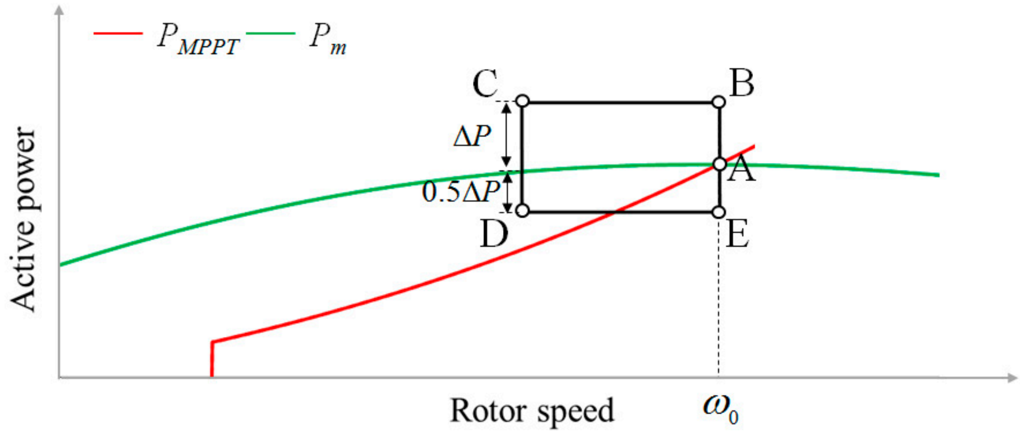


(**b**)

**Figure 3.** Power reference of SIC #1. (**a**) Power reference in the time domain; (**b**) Power reference in the rotor speed domain.

Implementation of SIC #2 may face several challenges, as follows: (I) after supporting the system frequency, a large amount of kinetic energy is fed to the grid, which extends the rotor speed convergence and further delays the rotor speed recovery. (II) Similar to SIC #1, $P_{ref}$ in the time domain may impose instability issues if a sudden disturbance occurs. (III) It is difficult to determine $\Delta P_{\mathrm{RR}}$ for the $\omega_r$ recovery stage to balance the rotor speed recovery and SFD. (IV) The $\Delta P$ only varies with operating conditions of the DFIG, but it is not suitable for various disturbances.

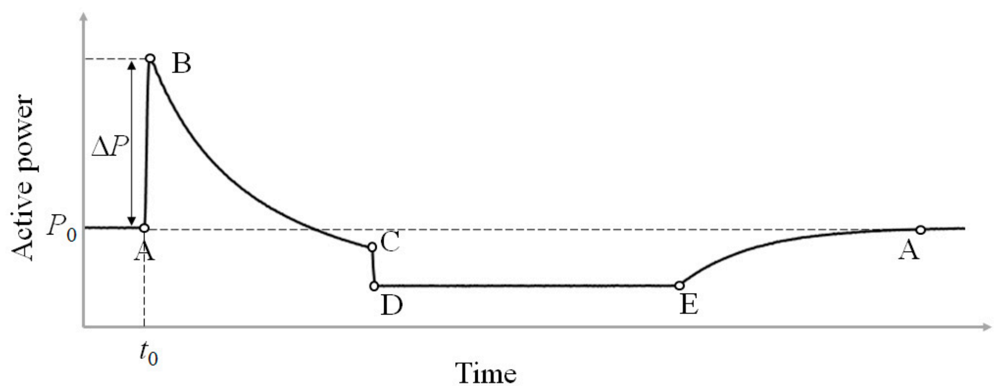


(**a**)

**Figure 4.** *Cont.*

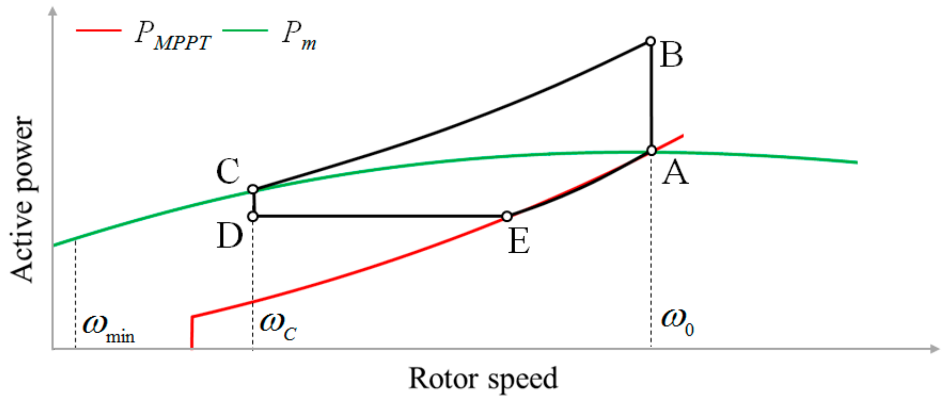

(**b**)

**Figure 4.** Power reference of SIC #2. (**a**) Power reference in the time domain; (**b**) Power reference in the rotor speed domain.

#### 3.1.3. SIC #3

SIC #3 increases the power reference from PMPPT to $\Delta P$ + PMPPT. Then, $\Delta P$ decreases with a linear ramp until $\Delta P$ decreases to zero so that PSIC meets the MPPT curve (B to C in Figure 5). After that, similar to SIC #2, the rotor speed is regained with the MPPT curve. The trajectory of SIC #3 is A–B–C–A, as shown in Figure 5. Similar to SIC #3, the rotor speed detector is bypassed.

$$P_{ref} = \begin{cases} P_{MPPT} + \Delta P[-\frac{1}{\Delta t}(t - t_0) + 1], & t_0^+ \leq t \leq t_C \\ P_{MPPT}, & t_C \leq t \end{cases} \tag{8}$$

where $\Delta t$ is the duration to meet the MPPT curve, and $t_c$ is the moment when $P_{ref}$ meets the MPPT curve.

Implementation of SIC #3 may face the following challenges: (I) after adding $\Delta P$, the output power decreases with a linear ramp, which is unable to improve the frequency stability sufficiently even though SIC #3 ensures the fast rotor speed recovery. (II) The $\Delta P$ only varies with operating conditions of the DFIG, but it is not suitable for various disturbances. The dynamic frequency supporting performance is restricted.

### 3.2. *Proposed Inertial Control for System Frequency Support*

The objectives for the proposed method are to boost the frequency nadir and guarantee the smooth $\omega_r$ recovery with a negligible SFD under various disturbances and wind penetrating levels. For these objectives, the proposed method defines the power reference into two stages: frequency supporting stage and rotor speed recovery stage.

During the frequency supporting stage, to boost the frequency nadir, the power reference during the frequency supporting stage increases up to $P_0$ + $\Delta P$, and then is maintained until the frequency nadir is detected (see trajectory A–B–C in Figure 6). Note that $\Delta P$ in the proposed method is derived on the basis of the maximum rate of change of frequency, $(df_{sys}/dt)_{\max}$, as in (9).

$$\Delta P = K \times \left(\frac{df_{sys}}{dt}\right)_{\max} \tag{9}$$

where $K$ is the weighting factor, which is determined based on the power system operating conditions.

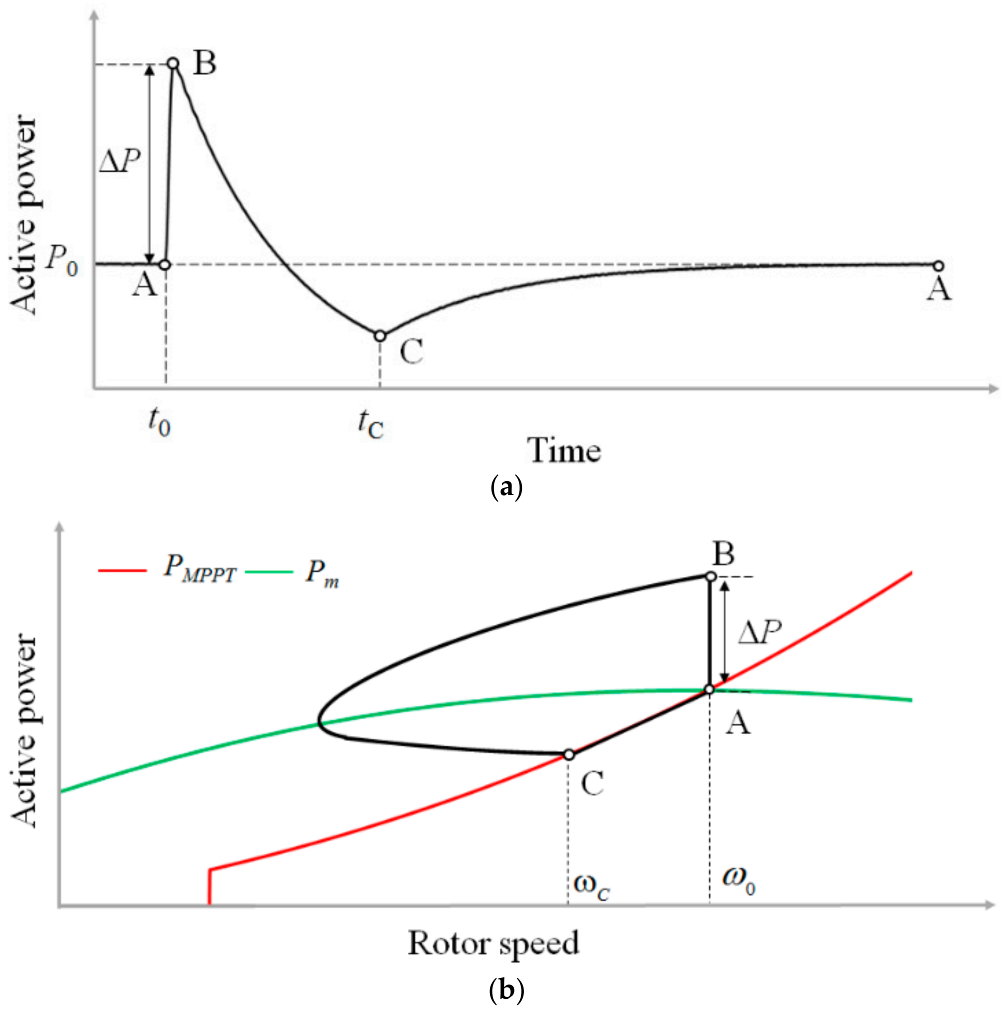


**Figure 5.** Power reference of SIC #2. (**a**) Power reference in the time domain; (**b**) Power reference in the rotor speed domain.

According to the swing equation of the power system [26,27], $df_{sys}/dt$, which is proportional to the power deficit (size of disturbance), has the maximum value at the instant of disturbance and decreases with time. As a result, $(df_{sys}/dt)_{\max}$ can reflect the size of the disturbance. Thus, the suitable $\Delta P$ can be derived under various disturbances by employing (8), whereas the fixed $\Delta P$ is employed for conventional SIC schemes. Further, such $\Delta P$ is maintained until the frequency nadir appears so as to boost frequency nadir, as shown in the trajectory A–B–C in Figure 6.

After that, the rotor speed recovery stage starts. To avoid the SFD, the instantaneous output power should be prevented [16]. To address this demand, a decreasing function is employed so as to smoothly decrease the output power, as shown the trajectory C-D-E in Figure 6. In detail, during the rotor speed recovery, $P_{ref}$ is designed as $P_{MPPT}$ + $\Delta P_{\mathrm{RR}}$, which is a linear decreasing function and decreases to zero for the predefined period, as in

$$\Delta P_{\mathrm{RR}} = \Delta P_{\mathrm{C}}[-\frac{1}{\Delta T}(t - t_0 - t_{FN}) + 1] \tag{10}$$

where $\Delta P_{\mathrm{RR}}$ indicates the power reduction during the rotor speed recovery stage and $\Delta P_{\mathrm{C}}$ represents $P_{SIC}(\omega_{\mathrm{c}}) - P_{MPPT}(\omega_{\mathrm{c}})$.

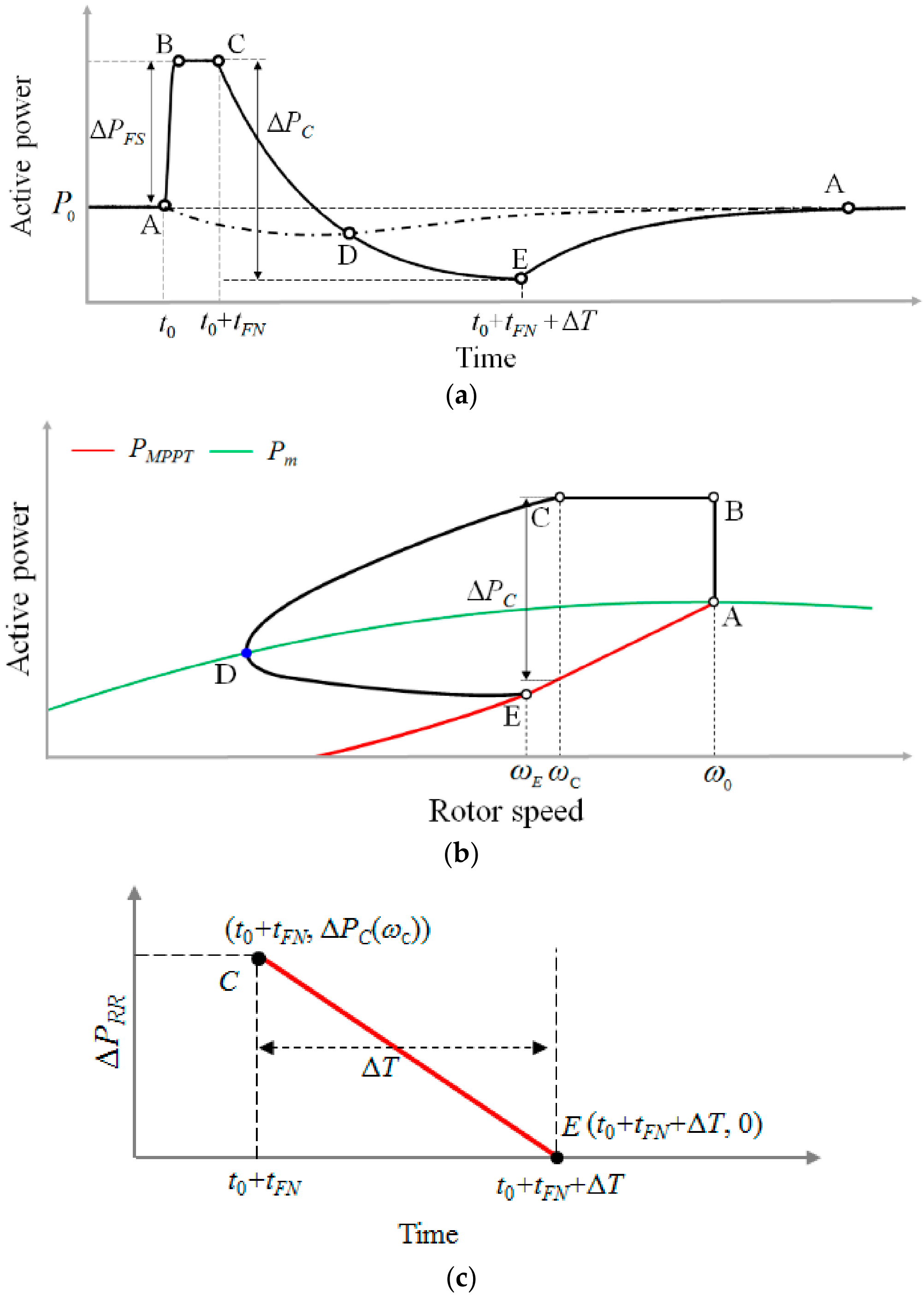


**Figure 6.** Power reference of the proposed scheme. (**a**) Power reference in the time domain; (**b**) Power reference in the rotor speed domain; (**c**) Regulation characteristics of $\Delta P_{RR}$.

Figure 6c shows the regulation characteristic of $\Delta P_{RR}$. During the initial period of rotor speed recovery, due to that $\Delta P_{RR}$ decreases with time, $\Delta P_{RR}$ is dominant during the rotor speed recovery, and the power reference smoothly decays; $P_m$ is less than $P_{ref}$ so that the rotor speed decreases. After Point D, $P_m$ is larger than $P_{ref}$ so that the rotor speed starts recovering. Until the operating point of the DFIG meets Point E, where rotor speed recovery ends, as in SIC #2 and SIC #3, $P_{SIC}$ is changed to $P_{MPPT}$. Thereafter, the DFIG recovers back to the initial operating condition. Hence, the duration for meeting the MPPT curve and size of an SFD are strongly dependent on the setting of $\Delta T$ in (9). If $\Delta T$ is a large value, the $\omega_r$

recovery is significantly slow, but it nearly avoids an SFD, and vice versa. This conclusion can be confirmed in Case 1 of the simulation results, which investigates the relationship between the size of the SFD, the rotor speed recovery, and $\Delta T$ by using different $\Delta T$.

The power reference of the proposed method in the time domain can be summarized as in (10).

$$P_{ref} = \begin{cases} P_0 + \Delta P & t_0 \le t \le t_0 + t_{\text{FN}} \\ P_{MPPT} + \Delta P_{RR} & t_0 + t_{\text{FN}} \le t \le t_0 + t_{\text{FN}} + \Delta T \\ P_{MPPT} & t_0 + t_{\text{FN}} + \Delta T \le t \end{cases} \quad (11)$$

Compared to the conventional SIC schemes, this proposed scheme could improve the frequency nadir determining the incremental power considering the maximum rate of change of frequency. In addition, the proposed scheme would smoothly decrease the power reference based on the decreasing function to minimize the SFD.

In this study, two detectors are used: a disturbance detector and a frequency nadir detector. The former switches $P_{ref}$ from $P_{MPPT}$ to the power reference for SIC if the frequency deviation exceeds 0.1 Hz; the latter is used to switch the reference function if the ROCOF meets the following condition:

$$\left|\frac{df}{dt}\right| \le 0.01\text{Hz/s} \quad (12)$$

## 4. Model System and Simulation Results

The proposed and conventional SIC schemes were implemented on a DFIG-based wind farm integrated to the model system (see Figure 7). The capacities of thermal synchronous generators G1, G2, G3, G4, G5, and G6 are 100 MVA, 100 MVA, 200 MVA, 200 MVA, 150 MVA, and 150 MVA, respectively. The motor load shares 62% of a total load of 534 MW. The motor load is a frequency-dependent load, which is able to respond to the dynamic frequency during a disturbance. Secondary frequency control is not considered, as the timeframe is long. Moreover, the system frequency for detecting a disturbance and the frequency nadir are calculated using a phase-locked loop.

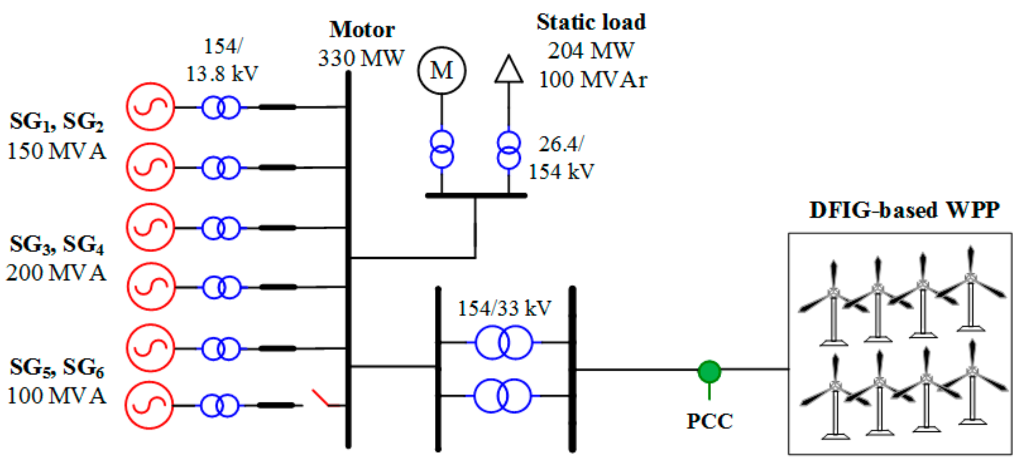


**Figure 7.** Single line model system with a 100-MW wind power plant.

In this section, four cases on a wind speed of 9.0 m/s are performed using EMTP-RV. As a disturbance, $G_6$, which generates 50 MW power to the grid for Case 1 and Case 2 and generates 90 MW power to the grid for Case 3 and Case 4, is tripped out from the grid at 40.0 s.

In this research, the results of the proposed method with different settings of $\Delta T$ are carried out to study the relationship between size of the SFD, the rotor speed recovery, and $a$ in Case 1. Moreover, several metrics including the frequency nadir, size of the SFD, and nadir-based frequency response are compared between the proposed method and the conventional methods in Case 2, Case 3, and Case 4.

### *4.1. Case 1: Wind Speed = 9.0 m/s, Disturbance = 50 MW, and Wind Penetration = 10% with Proposed SIC with Various ΔT*

In this case, three scenarios are considered to investigate the performance of the proposed method in terms of the rotor speed recovery and SFD when the setting of $\Delta T$ is set to different values. As shown in Figure 8, the red solid, green solid, and blue dotted curves indicate the results for the MPPT operation, the proposed method ($\Delta T$ = 10), the proposed method ($\Delta T$ = 15), and the proposed method ($\Delta T$ = 20), respectively.

As shown in Figure 8, the frequency nadirs for these three scenarios are the same, which are 59.671 Hz. This is because the same power is injected during the frequency support stage. During the rotor speed recovery stage, due to the various settings of $\Delta T$, the frequency rebounding response and rotor speed recovery of these three scenarios are different. The rotor speed reductions in the proposed method ($\Delta T$ = 10), the proposed method ($\Delta T$ = 15), and the proposed method ($\Delta T$ = 20) are 0.931 p.u., 0.918 p.u., and 0.907 p.u., respectively. Simulations results show that, with the large setting of $\Delta T$, the released kinetic energy is large and the durations to meeting the MPPT curve and rotor speed recovery are delayed, and vice versa. Further, due to the smoothing power reduction, there are no SFDs for these three scenarios of the proposed SIC scheme with various $\Delta T$. Hence, the proposed SIC is able to regulate the duration to meeting the MPPT curve and thus indirectly control the size of an SFD and time for the rotor speed recovery without the requirement of mechanical input power. Further, it is clearly observed that the setting of $\Delta T$ almost has a linear relation with the time to meet the MPPT curve.

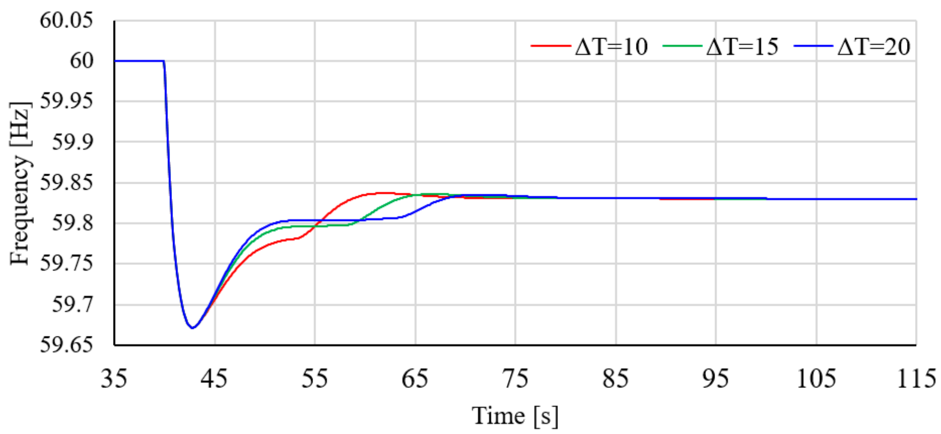


(**a**)

**Figure 8.** *Cont.*

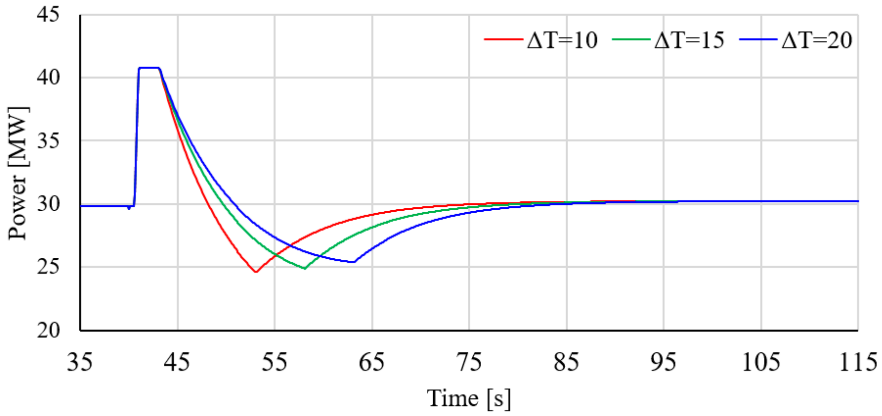


(**b**)

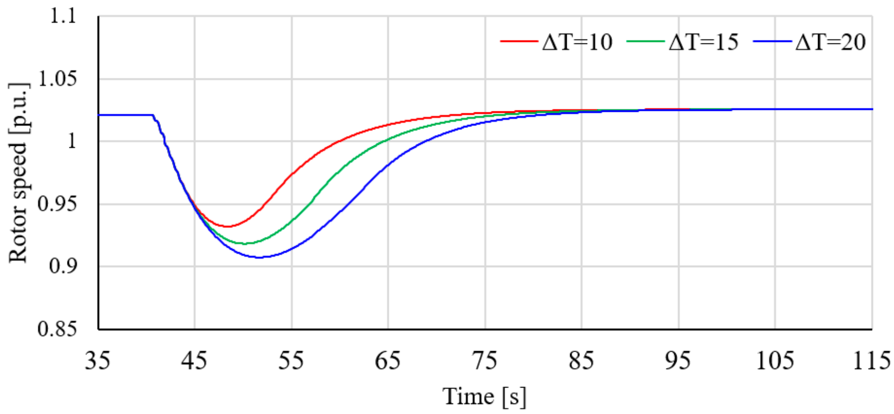


(**c**)

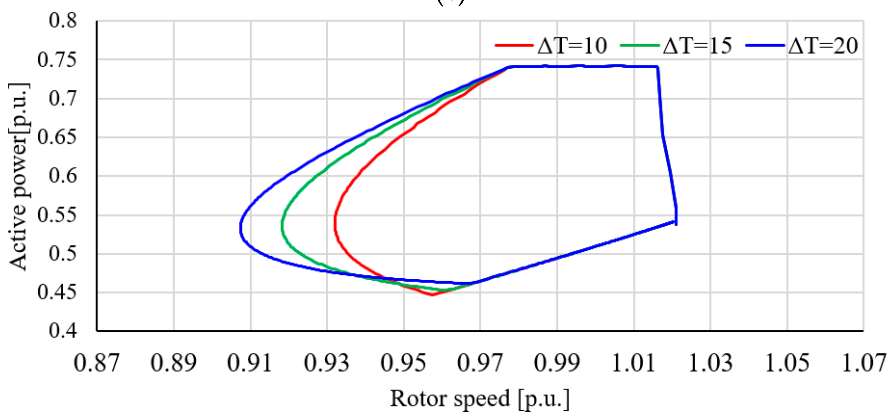


(**d**)

**Figure 8.** Results for Case 1. (**a**) System frequency; (**b**) Output power of the wind farm; (**c**) Rotor speed; (**d**) Output power in the rotor speed domain.

### *4.2. Case 2: Wind Speed = 9.0 m/s, Wind Penetration = 10%, and Disturbance = 50 MW with Different SIC Methods*

In this case, four scenarios are considered to investigate the performance of the dynamic frequency response. The ΔPs for the SIC #1, SIC #2, and SIC #3 are 0.1 p.u., 0.250 p.u., and 0.250 p.u., respectively. The ΔP for the proposed SIC scheme is 0.202 p.u. based on (8), and ΔT of the proposed SIC is set to 15.0 s.

As shown in Figure 9 and Table 1, the frequency nadirs for SIC #1, SIC #2, SIC #3, and the proposed method are 59.624 Hz, 59.669 Hz, 59.661 Hz, and 59.671 Hz, respectively. The nadir-based frequency responses for these methods are 133.0 MW/Hz, 151.1 MW/Hz, 147.5 MW/Hz, and 152.0 MW/Hz, respectively.

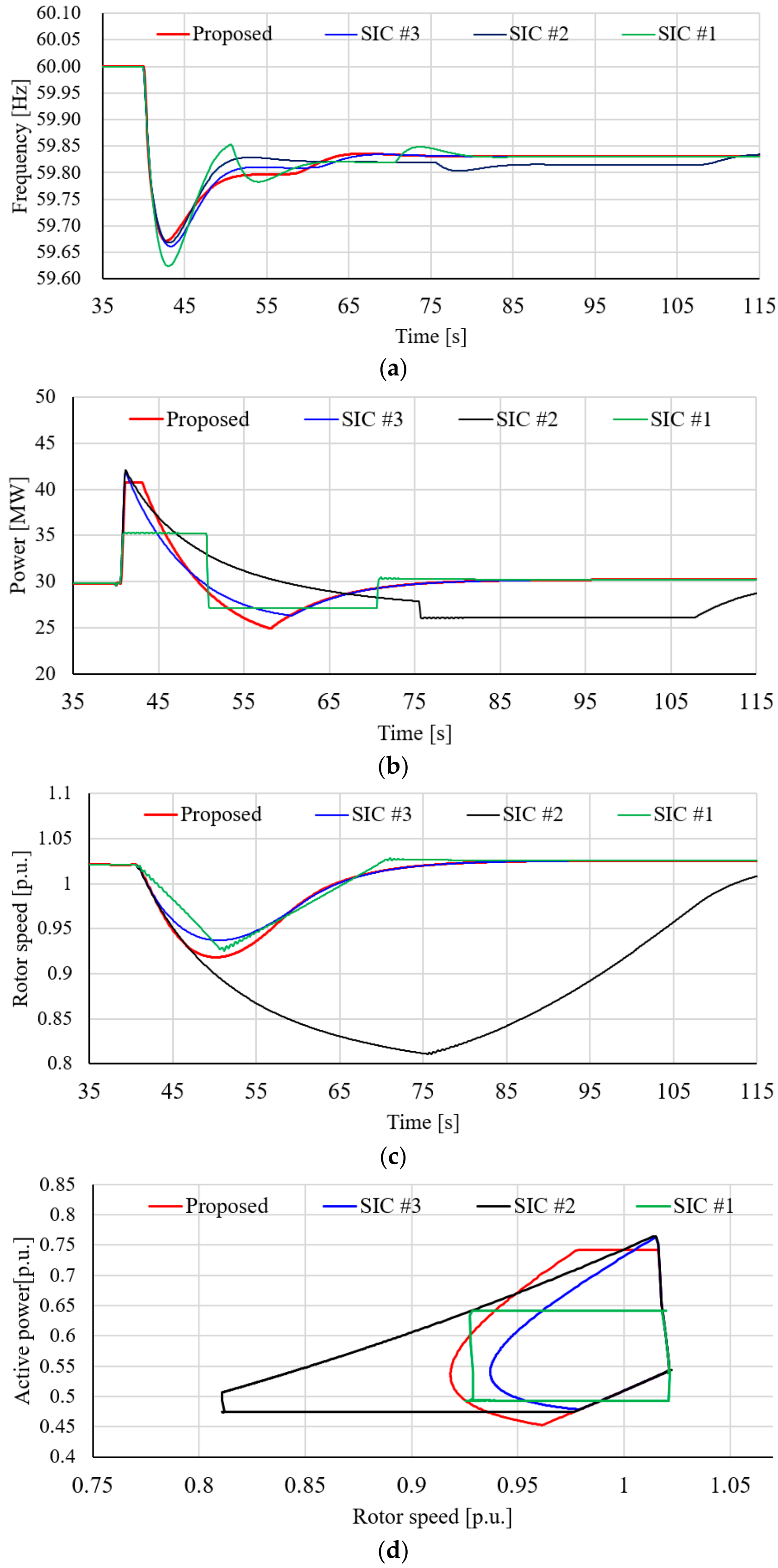


**Figure 9.** Results for Case 2. (**a**) System frequency; (**b**) Output power of the wind farm; (**c**) Rotor speed; (**d**) Output power in the rotor speed domain.

**Table 1.** Summary of Case 2, Case 3, and Case 4.

| | Methods | Case 2 | Case 3 | Case 4 |
|---|---|---|---|---|
| Frequency nadir (Hz) | SIC #1 | 59.624 | 59.266 | 59.255 |
| | SIC #2 | 59.669 | 59.308 | 59.35 |
| | SIC #3 | 59.661 | 59.303 | 59.338 |
| | Proposed SIC | 59.671 | 59.382 | 59.49 |
| Second frequency nadir (Hz) | SIC #1 | 59.783 | 59.655 | 59.549 |
| | SIC #2 | 59.803 | 59.666 | 59.577 |
| | SIC #3 | - | - | - |
| | Proposed SIC | - | - | - |
| Nadir-based frequency response (MW/Hz) | SIC #1 | 133 | 122.6 | 120.8 |
| | SIC #2 | 151.1 | 130.1 | 174.4 |
| | SIC #3 | 147.5 | 129.1 | 166.7 |
| | Proposed SIC | 152 | 145.6 | 177 |

For SIC #1, the frequency nadir of SIC #1 is 59.624 Hz. By injecting active power to the grid from the DFIG during the frequency support stage, it causes an SFD during the rotor speed recovery stage. The second frequency nadir is 59.782 Hz at 54.0 s due to the fast and large power reduction, which results in a large power imbalance for the power system based on the analysis of the swing equation. For SIC #2, due to the large amount of released kinetic energy, the minimum system frequency of SIC #2 is improved to 59.669 Hz. However, after supporting the frequency, a large level of kinetic energy is released to the grid so that the rotor speed convergence is delayed. In addition, a small power is reduced to ensure a small SFD but this results in a significantly slow rotor speed recovery and further impacts on the captured kinetic and wind generation efficiency. The SFD is caused due to the small power imbalance. The second frequency nadir is 59.803 Hz. The rotor speed reduction is 0.811 p.u., which is more than twice of SIC #1. For SIC #3, the minimum system frequency is 59.661 Hz, which is almost the same as in Case 2, however, it can prevent the SFD and release less kinetic energy since the output power smoothly decreases. For the proposed SIC method, even though a small incremental power is used, the frequency nadir is the highest since the proposed SIC method keeps the constant output power until the frequency nadir produces. Thus, the proposed SIC enables an effective method for sustaining the dynamic system frequency despite that the released kinetic energy is similar to those of SIC #1 and SIC #3.

### *4.3. Case 3: Wind Speed = 9.0 m/s, Wind Penetration = 10%, and Disturbance = 90 MW with Different SIC Methods*

In this case, a large disturbance of 90 MW is modeled to investigate the universality of the proposed SIC scheme. The parameters for SIC #1, SIC #2, and SIC #3 are set the same as in Case 2, however, $\Delta P$ for the proposed SIC is 0.327 p.u., which is more than in Case 2 due to the increased $(df_{sys}/dt)_{\max}$.

As shown in Figure 10 and Table 1, the frequency nadirs are 59.308 Hz, 59.303 Hz, and 59.382 Hz with SIC #2, SIC #3, and the proposed method, respectively. The NBFRs for these methods are 130.1 MW/Hz, 129.1 MW/Hz, and 145.6 MW/Hz, respectively. This is because the proposed SIC scheme increases the output power to 48.8 MW, whereas the other SIC schemes increase to 35.3 MW and 41.9 MW, respectively. Even if the injected energy for the proposed SIC scheme is almost the same as in SIC #2, the frequency nadir is significantly more than SIC #2. Furthermore, as in Case 2, the proposed SIC scheme ensures the smooth rotor speed without an SFD compared those with other SIC schemes.

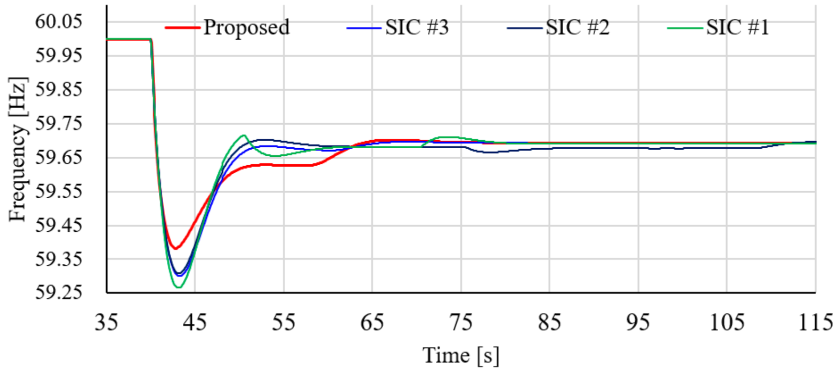


(**a**)

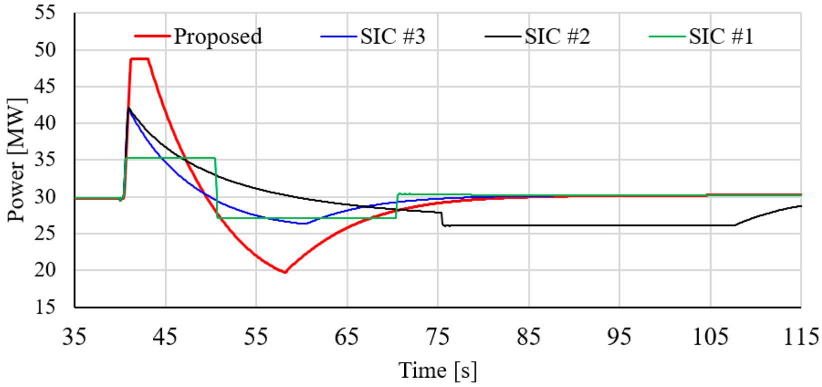


(**b**)

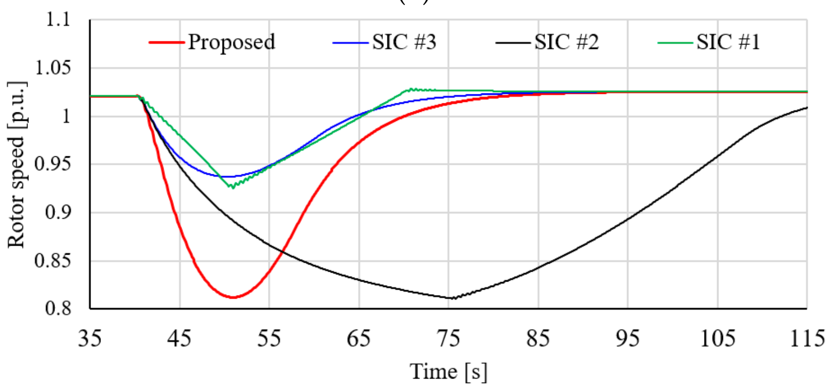


(**c**)

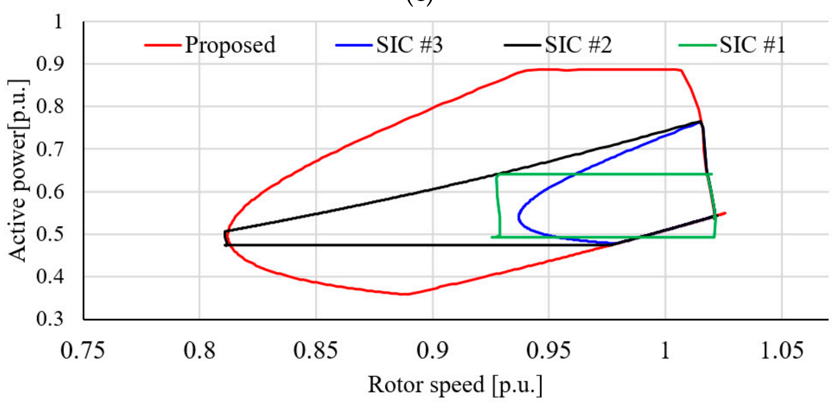


(**d**)

**Figure 10.** Results for Case 3. (**a**) System frequency; (**b**) Output power of the wind farm; (**c**) Rotor speed; (**d**) Output power in the rotor speed domain.

### 4.4. Case 4: Wind Speed = 9.0 m/s, Wind Penetration = 20%, and Disturbance = 90 MW with Different SIC Methods

In this case, for realizing the high wind penetration, the capacity of the wind farm increases to 110 MW and $G_5$ is set to be in standby mode. The parameters for SIC #1, SIC #2, and SIC #3 are set to the same as in Case 1 and Case 2, however, $\Delta P$ for the proposed SIC is 0.349 p.u., which is more than Case 3 due to the increased maximum $df/dt$.

As shown in Figure 11, the frequency nadirs are 59.350 Hz, 59.338 Hz, 59.329 Hz, and 59.490 Hz with SIC #1, SIC #2, SIC #3, and the proposed method, respectively. The NBFRs are 174.4 MW/Hz, 166.7 MW/Hz, 165.3 MW/Hz, and 177.0 MW/Hz, respectively, due to the large $\Delta P$ calculated by (9). Further, as in Case 3, even though the frequency rebounding response is relatively slow, the proposed SIC ensures the smooth rotor speed without an SFD compared those with other SIC schemes.

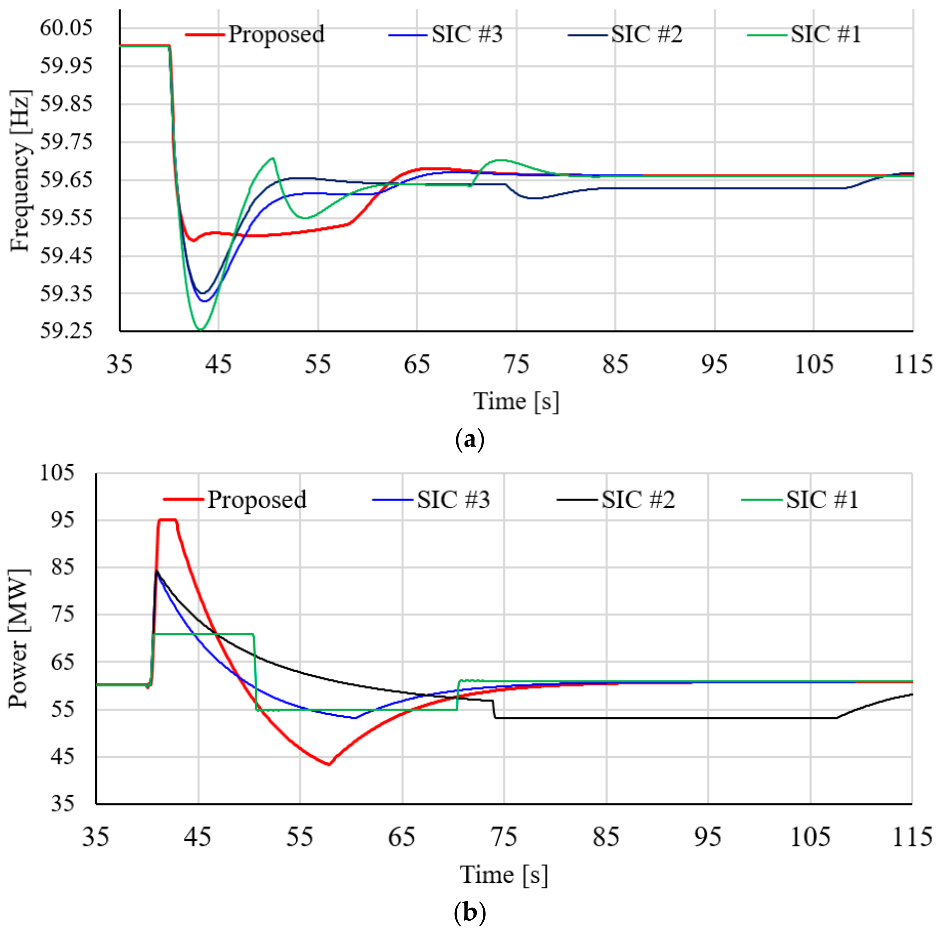


**Figure 11.** Results for Case 4. (**a**) System frequency; (**b**) Output power of the wind farm.

The more severe disturbance and higher wind power penetration result in larger maximum $df/dt$ so as to derive a large $\Delta P$ during the frequency supporting stage. This is the reason that the improvements of the frequency nadirs in Case 3 and Case 4 are more than in Case 2. Further, even though the smooth decay output power causes the late frequency rebounding, the proposed SIC scheme guarantees the smooth rotor speed recovery without an SFD.

## 5. Conclusions

This paper proposes a self-adaptive inertial control of a DFIG to reduce the maximum frequency deviation while smoothly regaining the rotor speed with a negligible SFD at the device level. The first objective is achieved by determining the incremental power considering the maximum rate of change of frequency; the secondary goal is realized by smoothly decreasing the power reference based on the decreasing function.

Simulation results indicate that the proposed SIC scheme provides better performance of boosting the frequency nadir compared to the conventional SIC methods, particularly for large disturbance with a high wind penetrating level. The proposed SIC method is capable of smoothly recovering $\omega_r$ without resulting in an SFD. Furthermore, the proposed SIC scheme is able to control the duration to meet the MPPT curve and thus indirectly regulating the size of an SFD and the rotor speed recovery. Simulation results sufficiently demonstrated the universality and effectiveness of the proposed self-adaptive inertial control scheme. Thus, the DFIG is a better option for system frequency support, as energy storage systems do, even though DFIGs operate in MPPT operation without any reserve power.

**Author Contributions:** X.X., J.H. and S.S. contributed to the conception and design of the proposed strategy. All authors wrote and edited the manuscript. All authors have read and agreed to the published version of the manuscript.

**Funding:** This work was supported by the Open Fund of State Key Laboratory of Operation and Control of Renewable Energy and Storage Systems (China Electric Power Research Institute) (No. NYB51202201698) and the Nantong Science and Technology Plan Project (grant number JC12022071).

**Data Availability Statement:** Data is available after requested.

**Conflicts of Interest:** The authors declare no conflict of interest.

## References

1. Kheshti, M.; Lin, S.; Zhao, X.; Ding, L.; Yin, M.; Terzija, V. Gaussian Distribution-Based Inertial Control of Wind Turbine Generators for Fast Frequency Response in Low Inertia Systems. *IEEE Trans. Sustain. Energy* **2022**, *13*, 1641–1653. [CrossRef]
2. Guo, X.; Zhu, D.; Hu, J.; Zou, X.; Kang, Y.; Guerrero, J.M. Inertial PLL of Grid-Connected Converter for Fast Frequency Support. *CSEE J. Power Energy Syst.* **2022**. [CrossRef]
3. Xiong, L.; Liu, L.; Liu, X.; Liu, Y. Frequency trajectory planning based strategy for improving frequency stability of droop-controlled inverter based standalone power systems. *IEEE J. Emerg. Sel. Top. Circuits Syst.* **2021**, *11*, 176–187. [CrossRef]
4. Abuagreb, M.; Ajao, B.; Herbert, H.; Johnson, B.K. Evaluation of Virtual Synchronous Generator Compared to Synchronous Generator. In Proceedings of the 2020 IEEE Power & Energy Society Innovative Smart Grid Technologies Conference (ISGT), Washington, DC, USA, 17–20 February 2020; pp. 1–5.
5. Duan, Q.; Zhao, C. Improved VSG Controlled SST in a Low-Voltage AC Distribution Network. In Proceedings of the 2021 IEEE Sustainable Power and Energy Conference (iSPEC), Nanjing, China, 25–27 November 2021; pp. 428–435.
6. Hydro Québec TransÉnergie. *Transmission Provider Technical Requirements for the Connection of Power Plants to the Hydro Québec Transmission System*; Hydro Québec: Montréal, QC, Canada, 2009.
7. National Grid UK. *Grid Code Review Panel Paper, Future Frequency Response Services*; National Grid: London, UK, 2010.
8. Yang, D.; Yan, G.-G.; Zheng, T.; Zhang, X.; Hua, L. Fast Frequency Response of a DFIG Based on Variable Power Point Tracking Control. *IEEE Trans. Ind. Appl.* **2022**, *58*, 5127–5135. [CrossRef]
9. Bao, W.; Ding, L.; Kang, Y.C.; Sun, L. Closed-loop synthetic inertia control for wind turbine generators in association with slightly over-speed deloading operation. *IEEE Trans. Power Syst.* 2023, *early access*. [CrossRef]
10. Xiong, L.; Liu, X.; Liu, H.; Liu, Y. Performance comparison of typical frequency response strategies for power systems with high penetration of renewable energy sources. *IEEE J. Emerg. Sel. Top. Circuits Syst.* **2022**, *12*, 41–47. [CrossRef]
11. Lyu, X.; Zhao, Y.; Groß, D.; Liu, T. Receding horizon control based secondary frequency regulation for power systems with wind energy integration. *Int. J. Electr. Power Energy Syst.* **2022**, *142*, 108282. [CrossRef]
12. Ye, Y.; Qiao, Y.; Lu, Z. Revolution of frequency regulation in the converter-dominated power system. *Renew. Sustain. Energy Rev.* **2019**, *111*, 145–156. [CrossRef]
13. Ullah, N.R.; Thiringer, T.; Karlsson, D. Temporary primary frequency control support by variable speed wind turbines—Potential and applications. *IEEE Trans. Power Syst.* **2008**, *23*, 601–612. [CrossRef]
14. Kheshti, M.; Ding, L.; Nayeripour, M.; Wang, X.; Terzija, V. Active power support of wind turbines for grid frequency events using a reliable power reference scheme. *Renew. Energy* **2019**, *139*, 1421–1454. [CrossRef]
15. Yang, D.; Kim, J.; Kang, Y.C.; Muljadi, E.; Zhang, N.; Hong, J.; Song, S.-H.; Zheng, T. Temporary frequency support of a DFIG for high wind power penetration. *IEEE Trans. Power Syst.* **2018**, *33*, 3428–3437. [CrossRef]
16. Lao, H.; Zhang, L.; Zhao, T.; Zou, L. Innovated inertia control of DFIG with dynamic rotor speed recovery. *CSEE J. Power Energy Syst.* **2022**, *5*, 1417–1427.
17. Hafiz, F.; Abdennour, A. Optimal use of kinetic energy for the inertial support from variable speed wind turbines. *Renew. Energy* **2015**, *80*, 629–643. [CrossRef]

18. Liu, K.; Qu, Y.; Kim, H.-M.; Song, H. Avoiding frequency second dip in power unreserved control during wind power rotational speed recovery. *IEEE Trans. Power Syst.* **2018**, *33*, 3097–3106. [CrossRef]
19. Kang, M.; Muljadi, E.; Hur, K.; Kang, Y.C. Stable adaptive inertial control of a doubly-fed induction generator. *IEEE Trans. Smart Grid* **2016**, *7*, 2971–2979. [CrossRef]
20. Yang, D.; Jin, Z.; Zheng, T.; Jin, E. An adaptive droop control strategy with smooth rotor speed recovery capability for type III wind turbine generators. *Int. J. Electr. Power Energy Syst.* **2022**, *135*, 107532. [CrossRef]
21. Fernandez, L.M.; Garcia, C.A.; Jurado, F. Comparative study on the performance of control systems for doubly fed induction generator wind turbines operating with power regulation. *Energy* **2008**, *33*, 1438–1452. [CrossRef]
22. Boukhezzar, B.; Siguerdidjane, H. Nonlinear control of a variable speed wind turbine using a two mass model. *IEEE Trans. Energy Convers.* **2010**, *26*, 149–161. [CrossRef]
23. Ajjarapu, V.; McCalley, J.D.; Rover, D.; Wang, Z.; Wu, Z. Novel Sensorless Generator Control and Grid Fault Ride-Through Strategies for Variable-Speed Wind Turbines and Implementation on A New Real-Time Simulation Platform. Ph.D. Dissertation, Department of Electrical and Computer Engineering, Iowa State University, Ames, IA, USA, 2010.
24. Abuagreb, M.; Allehyani, M.; Johnson, B.K. Design and Test of a Combined PV and Battery System under Multiple Load and Irradiation Conditions. In Proceedings of the 2019 IEEE Power & Energy Society Innovative Smart Grid Technologies Conference (ISGT), Washington, DC, USA, 17–20 February 2019; pp. 1–5.
25. Chauhan, U.; Singh, V.; Kumar, B.; Rani, A. An improved MVO assisted global MPPT algorithm for partially shaded PV system. *J. Intell. Fuzzy Syst.* **2020**, *38*, 6715–6726. [CrossRef]
26. Abuagreb, M.; Ajao, B.; Johnson, B.K. Implementation of Emulated Inertia using PV Generation with Energy Storage to Improve Integrated Grid Response. In Proceedings of the 2020 IEEE Texas Power and Energy Conference (TPEC), College Station, TX, USA, 6–7 February 2020; pp. 1–6.
27. Allehyani, M.F.; Abuagreb, M.; Johnson, B.K. The Effect of Frequency Droop Damping on System Parameters and Battery Sizing during Load Change Condition. In Proceedings of the 2022 International Conference on Electrical, Computer and Energy Technologies (ICECET), Prague, Czech Republic, 20–22 July 2022; pp. 1–5.